A Journal of the Gesellschaft Deutscher Chemiker

Angewandte International Edition GDCh Chemie

www.angewandte.org

Accepted Article

Title: "Turbo-Charged" DNA Motors with Optimized Sequence Enable Single-Molecule Nucleic Acid Sensing

Authors: Luona Zhang, Selma Piranej, Arshiya Namazi, Steven Narum, and Khalid Salaita

To be cited as: *Angew. Chem. Int. Ed.* **2024**, e202316851

Link to VoR: https://doi.org/10.1002/anie.202316851

WILEY VCH

10.1002/anie.202316851

WILEY VCH

RESEARCH ARTICLE

"Turbo-Charged" DNA Motors with Optimized Sequence Enable Single-Molecule Nucleic Acid Sensing

Luona Zhang[+[a]], Selma Piranej[+[a]], Arshiya Namazi[[a]], Steven Narum[[b]], Khalid Salaita*[[a], [b]]

[a] L. Zhang, S. Piranej, A. Namazi, Prof. K. Salaita
Department of Chemistry, Emory University
Atlanta, GA 30322 (USA)
Email: k.salaita@emory.edu

[b] S. Narum, Prof. K. Salaita
Wallace H. Coulter Department of Biomedical Engineering, Georgia
Institute of Technology and Emory University
Atlanta, GA 30322 (USA)

[+] These authors contributed equally to this work.

Supporting information for this article is given via a link at the end of the document.

Abstract: DNA motors that consume chemical energy to generate processive mechanical motion mimic natural motor proteins and have garnered interest due to their potential applications in dynamic nanotechnology, biosensing, and drug delivery. Such motors translocate by a catalytic cycle of binding, cleavage, and rebinding between DNA "legs" on the motor body and RNA "footholds" on a track. Herein, we address the well-documented trade-off between motor speed and processivity and investigate how these parameters are controlled by the affinity between DNA legs and their complementary footholds. Specifically, we explore the role of DNA leg length and GC content in tuning motor performance by dictating the rate of leg-foothold dissociation. Our investigations reveal that motors with 0% GC content exhibit increased instantaneous velocities of up to 150 nm/sec, three-fold greater than previously reported DNA motors and comparable to the speeds of biological motor proteins. We also demonstrate that the faster speed and weaker forces generated by 0% GC motors can be leveraged for enhanced capabilities in sensing. We observe single-molecule sensitivity when programming the motor to stall in response to the binding of nucleic acid targets. These findings offer insights for the design of high-performance DNA motors with promising real-world biosensing applications.

Introduction

Biological motors, such as myosin, kinesin, and dynein, consume chemical energy stored in ATP molecules to power mechanical functions essential to life, including the locomotion of cells, muscle contraction, and intracellular cargo transport.[1,2] Chemists have long sought to create synthetic motors that autonomously operate under conditions far-from-equilibrium to processively harness chemical energy as these machines are envisioned to have broad applications ranging from biosensing, to creating synthetic cells and molecular computation. Among the various molecular motors developed to date, the ones made of DNA hold the greatest potential because they are highly modular, facile to create, and programmable using Watson-Crick-Franklin base pairing rules.[3-6] Indeed, the fastest and most processive DNA motors, reported to date, are the rolling motors comprising of micro-[7-9] or nano-scale[10,11] scaffolds functionalized with single stranded DNA (ssDNA) "legs" complementary to a monolayer of single stranded RNA (ssRNA) "fuel" that serves as the track. Processive motion can be initiated and powered by the enzymatic hydrolysis of the bound fuel. Rolling motors which have been created using silica and polystyrene microparticles, inorganic nanoparticles, DNA origami structures with isotropic and anisotropic geometries all require high multivalency, a rapid "step" rate driven by catalytic cycles of binding-hydrolysis-unbinding, and a rigid chassis that coordinates leg movement. These criteria have demonstrated the ability to prompt rapid translocation down a self-created gradient of chemical fuel at micrometer-per-minute speeds with a persistence that can lead to ~millimeter displacements.

A fundamental question in this area pertains to how one can further enhance the speed of DNA motors while maintaining high processivity. This is a critical goal as DNA motors have already shown exciting potential in molecular computation[9] and sensitive viral detection[12], and enhancing motor speed will improve the performance and capabilities of rolling motors in such applications. Indeed, our past modeling predicts that a high baseline velocity provides two key advantages: an increased sampling frequency of target molecules and a more pronounced change in speed upon target-induced mechanical stalling events. However, previous experimental and theoretical work studying synthetic motors exposed a dilemma where an increase in motor speed sharply leads to diminished processivity.[13-17] This trade-off arises because as the rate of forward "stepping" or enzymatic hydrolysis of footholds is increased, the probability of spontaneous detachment of the motor from the surface will also increase.[18,19] This is intuitive as any transient duration where all the DNA legs are unbound will lead to motor dissociation from the track. Past work tuning the enzyme concentration to modulate k_{off} of DNA

10.1002/anie.202316851
WILEY VCH

RESEARCH ARTICLE

legs confirmed this relationship.[7,10] However, one aspect of rolling motors that has not yet been explored relates to the free energy of hybridization (ΔG_{hybrid}) between the DNA leg and their complementary foothold RNA. Here, we postulate that the speed-processivity trade-off limitations may be overcome by tuning leg-foothold affinity as it modulates multiple parameters simultaneously, including k_{on}, k_{off}, and k_{cat}. Other DNA-based technologies, such as DNA-PAINT, that depend on rapid and reversible binding events, underscore the importance of tuning DNA binding affinity and kinetics in overall assay performance.[20,21]

Herein, we investigate how the thermodynamic and kinetic properties of DNA leg-RNA foothold binding (k_{on}), cleavage (k_{cat}), and dissociation (k_{off}) can drastically tune the emergent properties of motor performance in terms of net displacement, velocity, processivity, and sensing. We demonstrate that DNA leg length and GC content follow the expected trade-off between speed and processivity. However, we found that lowering the GC content to 0% leads to motors that travel at average speeds that are 8-fold greater than that of the original DNA leg sequence with 33% GC content with only a marginal loss in processivity at optimized buffer conditions. Kinetics measurements suggest that this is the result of enhanced k_{off} despite a similar k_{cat} rate for the 0% GC DNA legs compared to the 33% GC content of the original sequence. Importantly, we found that these optimized 'turbo-charged' motors with 0% GC content display peak velocities of 150 nm/sec, closely approaching the speed of biological motor proteins.[22-24] Turbo-charged motors can serve as improved sensors using a chemical-to-mechanical transduction mechanism based on stalling in response to single nucleic acid targets. Thus, sequence optimization allows for the single-molecule detection of oligonucleotide targets, which was previously not accessible.

Results and Discussion

Effect of DNA leg length on motor performance

Rolling DNA motors are driven by a self-sustaining chemical gradient which we previously described as autochemophoresis.[8] In this work, motors were generated using spherical silica microparticles functionalized with a dense monolayer of single-stranded DNA that hybridizes to complementary Cy3-labeled single-stranded RNA immobilized onto a gold chip (**Figure 1A**). Upon RNase H addition, RNA in RNA:DNA duplexes is cleaved, creating a differential in the energy landscape between the motor current position and adjacent positions. DNA legs then rebind to fresh RNA fuel sites, enabling rolling in a "burnt-bridge" ratchet mechanism with multiple turnover kinetics through a repetitive series of binding-hydrolysis-unbinding cycles. Loss of the Cy3 label allows for the visualization of RNA fuel consumption in the wake of the motor. Tight binding between DNA legs and RNA fuel (ΔG_{hybrid}) is a prerequisite for maintaining high processivity, as weak binding likely leads to transient dissociation of the motor from the chip and diminished processivity (**Figure 1B**). Conversely, strong DNA leg-RNA fuel binding is expected to slow k_{off} and hence lead to diminished motor velocity. Hence, the rational design of a faster DNA motor entails striking a delicate balance as to tune the ΔG_{hybrid} between DNA legs and RNA fuel while maintaining processivity and optimizing speed.

There are a few interconnected factors (e.g., oligonucleotide sequence, complementarity, and melting temperature of the duplex) that can exercise control over ΔG_{hybrid} and, hence, are expected to affect the kinetics involved in the "cog-and-wheel" mechanism. We were first interested in determining whether changing the length of the DNA leg would alter motor performance

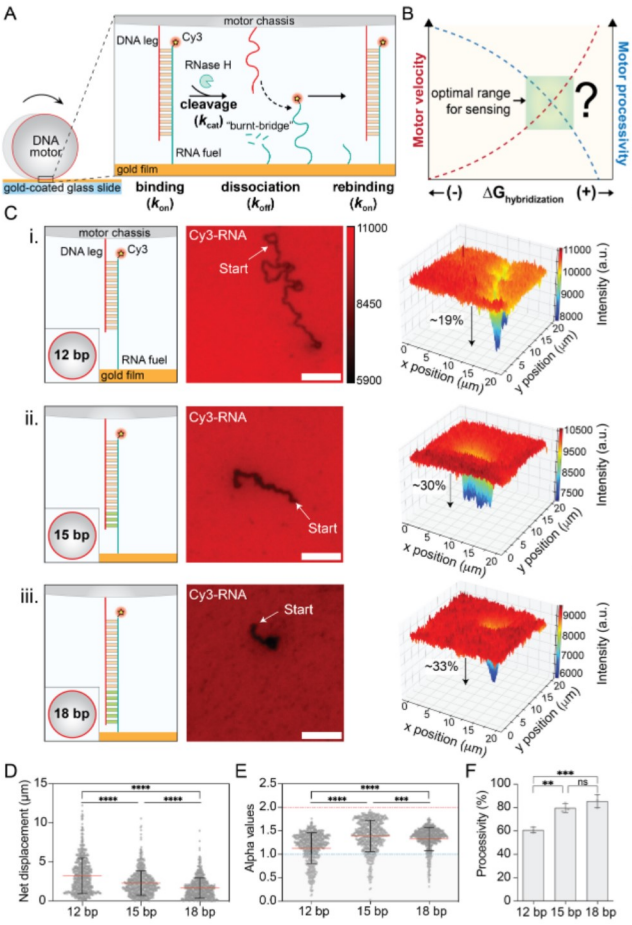

Figure 1. Determining the effect of DNA leg length on motor performance. A) Schematic of the DNA-based motors rolling on the RNA-coated gold film. DNA-legs bind to their complementary RNA fuel footholds, and exhibit "burnt-bridge" Brownian motion upon the addition of the RNase H enzyme which selectively cleaves duplexed RNA. Once the DNA leg is released from the cleaved RNA fuel foothold sites, the DNA leg then bind to new RNA fuel sites. B) A theoretical plot of the relationship between motor velocity, processivity and $\Delta G_{hybridization}$ between DNA legs and RNA footholds. This work focuses on finding the optimal range between these three variables for sensing applications. C) Representative fluorescence imaging of the DNA-based motors modified with leg lengths of 12 (**i**), 15 (**ii**), and 18 (**iii**) nucleotides (nt) and their depletion tracks (at t = 30 min after RNase H addition). The RNA fuel was tagged with Cy3, shown here in red. The vertical color bar indicates the fluorescence intensity values (a.u.) and applies to the images shown in (**i**), (**ii**) and (**iii**). The scale bar is 5 μm. For each image in **i-iii** we also show a 3D fluorescence intensity plot of the entire ROI indicating a 19% decrease in fluorescence for the motors modified with 12 bp DNA legs, 30% decrease for motors with 15 bp DNA legs, and 33% decrease for motors with 18 bp DNA legs. The 3D fluorescence intensity plots are color-coded based on the fluorescence intensity values. D) Plot showing net displacement of over 300 motors modified with 12, 15, and 18 bp DNA legs. E) Plot of α values of over 300 motors modified with 12, 15, and 18 bp DNA legs. F) Plot showing % processivity of motors modified with 12, 15, and 18 bp. Points represent the % processivity of each individual replicate and the error bars show the standard deviation. ns, **, *** and **** indicate not statistically significant, P<0.01, P<0.001 and P<0.0001, respectively. Experiments were performed in triplicate.

to the same extent as in other DNA-based technologies. For this, we tested three types of motors differentiated by varying the DNA leg lengths on the motors: 12, 15, and 18 base pairs (bp) which correspond to ΔG_{hybrid} of -17.8 kcal/mol, -21.08 kcal/mol, and -31.9 kcal/mol at 25˚C and 137 mM NaCl, respectively (**Figure 1C**). The motors were treated with the same RNase H buffer conditions including 0.05 units/µl of enzyme and 10% formamide (v/v). When the length of the DNA:RNA hybrid was set to 12 bp, we observed long depletion tracks in the Cy3-RNA fluorescence channel compared to the 15 and 18 bp design. By analyzing the intensity profile of a single track, we found that ~19% of the Cy3-RNA fuel was depleted by the 12 bp motor. The percentage of depleted or consumed fuel increased to ~30% and ~33% when forming 15 and 18 bp hybrids, respectively. This reduction in the fraction of cleaved RNA with increased depletion track lengths is consistent with the 12 bp duplex displaying a greater k_{off} rate that may allow motion without cleavage of RNA substrate.

We next performed brightfield particle tracking to analyze motor net displacement, type of motion, and processivity on hundreds of motors (**Supplementary Figure 1).** This analysis showed that the 12 bp motors display enhanced net displacements compared to the 15 and 18 bp designs, further corroborating the enhanced k_{off} rate as dissociation can occur with fewer cleavage events (**Figure 1D**). The 15 bp motors showed a 65% increase in net displacement compared to the 18 bp motors with 0.05 units/µl of RNase H. Because a longer duplex will require more individual cleavage events to yield complete tether dissociation, we incubated the 18 bp motors with higher enzyme concentrations. We observed that doubling the enzyme concentration to 0.1 units/µl led to an increase in the net displacement (2.4 +/- 1.6 µm), comparable to that of the 15 bp motor with 0.05 units/µl of enzyme (**Supplementary Figure 2**).

As expected, the processivity was greatly dampened as the ΔG_{hybrid} of DNA:RNA binding was reduced. One parameter to quantify the super-diffusive nature of these motors is the power law dependence between the mean square displacement (MSD) and the lag time ($MSD \propto \tau^{\alpha}$).[25] The scaling exponent α (alpha) gives a value of 1 for random Brownian diffusion (linear dependence), <1 for sub-diffusive motion, and >1 for super-diffusive motion. This diffusional coefficient is also an excellent indicator of motor processivity as detachment from the track abolishes the self-avoiding bias. The 15 bp and 18 bp motors showed α of 1.4 and 1.3, respectively, indicating mostly super-diffusive motion. In contrast, the 12 bp motors displayed Brownian motion with an average α= 1.1 +/- 0.3 (**Figure 1E**). To validate this conclusion, we also quantified the ratio of particles colocalized with their tracks to the total number of tracks detected (here defined as 'processivity %'), which dropped from ~80% (15 and 18 bp) to ~60% for 12 bp motors (**Figure 1F)**. Consistently, further shortening of the oligonucleotides down to 9 bp caused a complete loss of processivity and absence of depletion tracks, and even upon withholding the denaturant in the rolling buffer which is expected to stabilize the DNA:RNA duplex (**Supplementary Figure 3**). Taking these results into account, the 15 bp sequence was chosen for further manipulation of ΔG_{hybrid} as it offered comparable processivity to the 18 bp design while achieving greater motor speed.

Effect of DNA sequence on motor performance

Next, we tuned the sequence of the 15 bp design which contained 33% GC base pairs and created two variants with GC content of 0% and 100% (**Figure 2A**). Because RNase H exhibits a distributive endonuclease activity and indiscriminately cleaves within the RNA substrate with multiple turnover, the distribution of GC base pairs was not considered a significant factor affecting motor performance.[26,27] Initially, we treated the motors with the same buffer conditions that included 0.05 units/µl of enzyme and 10% formamide (v/v). However, we found that these two types of motors were not compatible with the same buffer composition. The 0% GC motors were not processive and exhibited hopping behavior while the 100% GC motors were processive but moved sluggishly with submicron distances. Thus, we had to adjust the conditions of the buffer for each motor design accordingly. The hypothesis guiding our optimization of the 0% GC design was that the rate of leg dissociation (k_{off}) was faster than the rate of forming new contacts with the surface RNA (k_{on}), causing transient dissociation (hopping) instead of processive rolling (**Supplementary Figure 4A**). Reducing the enzyme concentration by 5-fold did not boost the α value (~1), and motors displayed Brownian motion across a range of concentrations from 0.05 to 0.01 units/µl of RNase H (**Supplementary Figure 4B**). Conversely, we achieved a noteworthy shift from Brownian motion to super-diffusive motion (α=1.35) by withholding the denaturant, formamide, from the buffer (**Supplementary Figure 4C**). The increase in net displacement as formamide was reduced from 2.5% to 0% v/v is likely due to switching of the motion into self-avoiding. Brightfield and fluorescence microscopy images showed long depletion tracks and improved colocalization between tracks and particle locations at these optimized conditions further validating the enhanced processivity (**Figure 2A**, **Supplementary Figure 4D**).

For the 100% GC design we hypothesized that the barrier to rolling was most likely due to the formation of hairpin secondary structures in single-stranded oligonucleotides (**Supplementary Figure 5A**). Specifically, we predicted that this secondary structure creates an energy barrier for DNA leg binding to complementary RNA fuel, thus blocking the "cog-and-wheel" mechanism. As shown in **Supplementary Figure 5B**, a series of different buffer conditions consisting of varying enzyme and formamide concentrations was screened for processive rolling (i.e., net displacement>0 µm and α>1). Sub-diffusive or Brownian motion was invariably observed at all enzyme concentrations and formamide concentrations below 30% v/v. Indeed, in the absence of formamide, the vast majority of particles did not bind to the surface (**Supplementary Figure 5C**). At 30% formamide concentrations and greater, motors bound to the surface and switched to active self-avoiding motion, validating the role of hairpin formation in hindering motion. Furthermore, pre-incubating the motors with formamide before initiating motion also led to enhanced processivity and an increase in α which supports the importance of destabilizing the hairpin in allowing for active translocation (**Supplementary Figure 5D**). The motor behavior observed in the 100% GC design indicates the importance of binding kinetics in dictating motor speed, as the 15 bp DNA:RNA

10.1002/anie.202316851
WILEY-VCH

RESEARCH ARTICLE

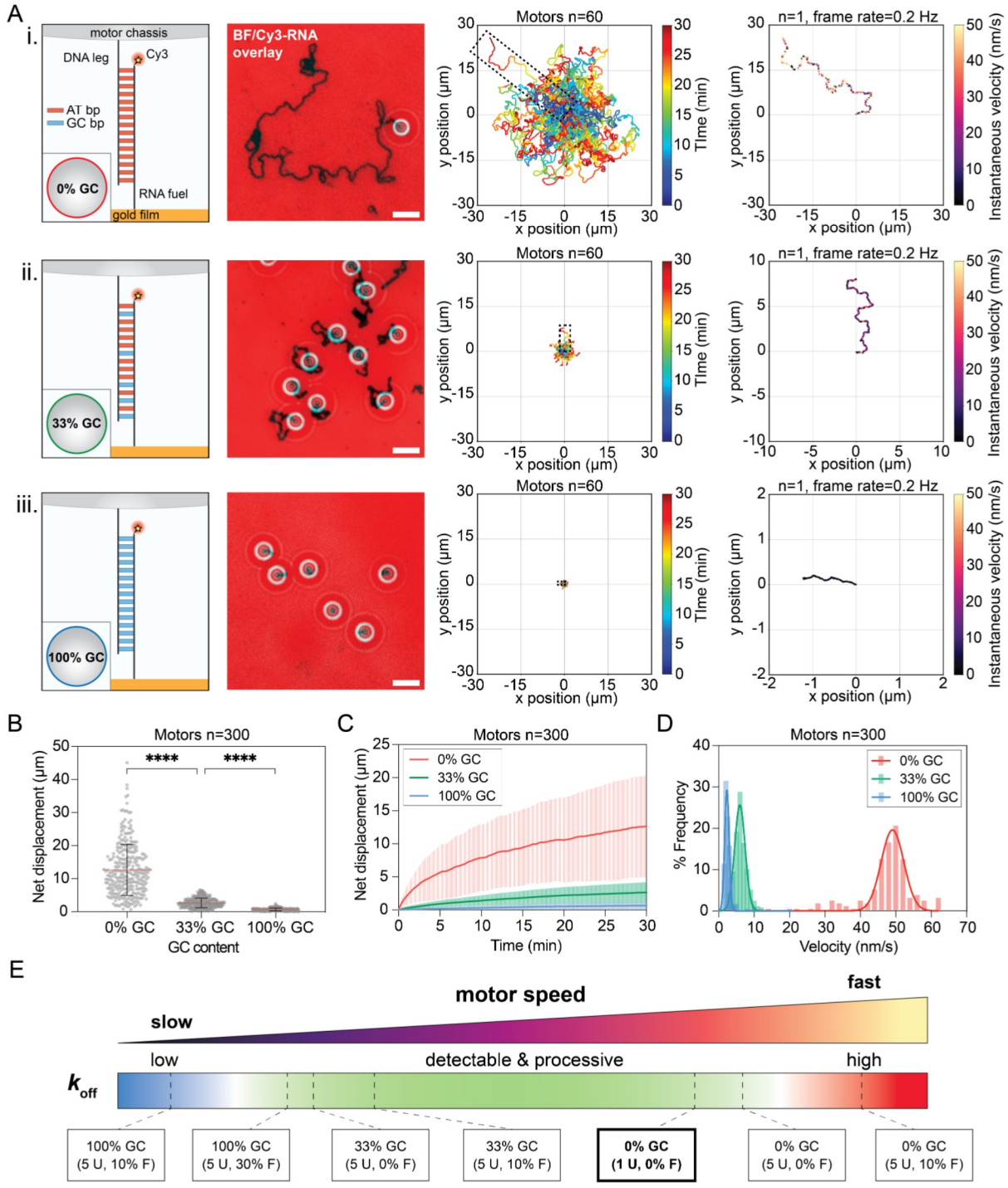

Figure 2. Determining the effect of sequence on motor performance. A) Representative overlay of brightfield and fluorescence imaging of motors with DNA legs consisting of 0% (**i**), 33% (**ii**), and 100% (**iii**) GC content and their depletion tracks (at t = 30 min after RNase H addition). The RNA fuel was tagged with Cy3, shown here in red. The scale bar is 5 μm. Plots showing the trajectories of 60 motors modified with 0% (**i**), 33% (**ii**), and 100% (**iii**) GC content. All the trajectories are aligned to the 0,0 (center) of the plots for time = 0 min. Color indicates time (0 → 30 min). Plots showing the instantaneous velocities of the selected trajectory for motors modified with 0% (**i**), 33% (**ii**), and 100% (**iii**) GC content. The trajectories are aligned to the 0,0 (center) of the plots and color indicates the instantaneous velocity over time (0 → 30 min). The frame rate used is 0.2 Hz. B) Plot showing net displacement of 300 motors modified with 0%, 33%, and 100% GC content. **** indicates P<0.0001. The error bars and the red lines represent the standard deviation and the mean of the distribution from triplicate experiments. C) Plot of net displacement over time of 300 motors modified with 0%, 33%, and 100% GC content. The shaded region represents the 95% confidence interval. D) Plot showing the frequency distribution of the velocity for 300 motors modified with 0%, 33%, and 100% GC content. E) Color-coded gradient bar summarizing how k_{off} influences motor speed and processivity as a result of different motor designs and buffer conditions. The 0% GC motors with 1 U of enzyme and 0% formamide (v/v) offer improved conditions for sensing with high k_{off} and speed and maintain processivity.

hybrid is at least 8-fold more thermodynamically stable than the intramolecular hairpin (**Supplementary Figure 6A, B**). When hairpins are predominant in both DNA legs and RNA fuel strands, DNA:RNA duplexes (the thermodynamic product) primarily form through toehold-mediated strand displacement reactions, which are notoriously slow.[28,29] This suggests that active motion may be present but at massively slowed rates. We tested this prediction by using fluorescence imaging to monitor depletion track formation at t~24 hrs after enzyme addition and noted the appearance of tracks even at [formamide] below 30% v/v (**Supplementary Figure 6C**).

After optimizing the buffer conditions, we then compared the impact of the GC content on motor performance. We used a standardized 30-min duration and visualized motion using brightfield and fluorescence microscopy (**Figure 2A**). The 0% GC motors generated longer depletion tracks compared to motors having greater GC content as seen in the Cy3-RNA fluorescence channel. This is likely because of enhanced k_{off} rates for the 0% GC sequence. Brightfield particle tracking confirmed that the 0% GC motors exhibited longer trajectories, with some motors approaching a net displacement of 20 μm in the 30-minute timelapse period. The trend was followed by the 33% GC and 100% GC motors, respectively **(Supplementary Movie 1)**. As expected, all three motor designs were immobile on the RNA chip without the addition of enzyme in the reaction buffer (**Supplementary Figure 7**). Analysis of motor instantaneous velocities further validated the enhanced speeds of the 0% GC motors. A representative trajectory was selected for each of the motors and color-coded based on the instantaneous velocity between consecutive frames (**Figure 2A**). We observed that the 0% GC motors can travel with average speeds of ~50 nm/s and peak velocities up to 150 nm/s (**Supplementary Figure 8**). Analysis of the net displacements of ~600 motors from triplicate measurements showed that the 0% GC motors traveled distances ~5-fold greater than that of the 33% GC motors and underscores the importance of ΔG_{hybrid} in tuning motor speed (**Figure 2B, Supplementary Movie 2**). Furthermore, the sustained increase in average net displacement over time is consistent with biased self-avoiding motion, which is achieved in all three model designs (**Figure 2C, Supplementary Figure 9**). Most importantly, the average velocity decreased from 49.08 (±3.19) to 5.97 (±1.48) and 2.28 nm/s (±0.64) with increasing GC content (**Figure 2D**). By testing an additional motor sequence with 13% GC content, we confirmed that this parameter tunes the motor speed in a non-linear fashion with the most dramatic variations in the range between 0% and 33% GC and maximization of motor speed at 0% GC (**Supplementary Figure 10**). Therefore, we dubbed these motors as 'turbo-charged' because of their enhanced speed relative to other sequences studied here, and thus allowing for velocities approaching that of biological motor proteins, such as kinesins that travel at 20-200 nm/s (**Figure 2E**).

We wondered why the 0% GC motors display 8-fold enhancement in average motor speed compared to that of the 33% GC motors. Surface kinetics of RNase H demonstrated that the enzymatic activity is lower in the 0% GC and 100% GC designs compared with the 33% GC benchmark when using the same buffer conditions (**Supplementary Figure 11**). Again, the reduction in substrate concentration is caused by either spontaneous leg dissociation or hairpin formation. These findings point toward the k_{off} rate as the key parameter that is driving the enhanced motors speeds. We postulate that fewer cleavage events are required to release the DNA leg from RNA footholds. This is consistent with our prior modeling that showed that increasing the cleavage rate of DNA leg:RNA fuel duplexes will enhance the speed of the motor in a non-linear fashion. Taken together, these results suggest that the turbo-charged motors move faster despite the dampened k_{cat}, and that the leg dissociation (k_{off}) is the kinetic bottleneck and rate-determining step of the rolling mechanism of the motors.

Programming "turbo-charged" motors for sensing

We next aimed to use the turbo-charged motors for mechanosensing of DNA analyte. By mechanosensing, we mean that the capture of analyte that binds both the motor and the chip leads to mechanical stalling of motion and hence transducing the chemical event into a mechanical signal. Our past modeling showed that the most desirable motor properties for effective mechanosensing are high speed which ensures that the target molecules are sampled at a high rate, and low force generation such that a smaller number of target molecules can stall the motors without being ruptured (**Figure 3A**).[13] We considered the magnitude of the forces associated with motor translocation which is dependent on the transient number of DNA:RNA tethers and ΔG_{hybrid}. Our results indicate that on average the turbo-charged motors consume ≤ 20% of RNA fuel and this is likely due to the reduced number of motor-surface junctions at any given time (**Supplementary Figure 12**). Therefore, this would suggest that the forces of the motor (F_{motor}) pulling the chassis forward to new RNA fuel are relatively weak. As a result, turbo-charged motors are expected to be highly sensitive to resistive forces applied against motion (**Figure 3A**). To test their mechanical sensitivity, we replaced a fraction of RNA fuel strands with a DNA analog that serves as the target of interest (TOI) (**Supplementary Figure 13**). This way, the encounter between the motor legs and TOI strands leads to the formation of RNase H-insensitive dsDNA junctions with the surface, generating a tunable resistance $F_{stalling}$ that competes with the F_{motor} to dictate whether motors move or stall (**Figure 3B**).

The mechanical sensitivity of the turbo-charged motors was tested on surfaces with 0%, 0.001%, 0.01%, 0.1% and 1% DNA probes, which correspond to estimated densities of 0, 0.5, 5, 50, and 500 probes/μm^2, respectively. To help with visualization of these TOIs on the RNA chip, we used gold nanoparticles functionalized with complementary ATTO647N-labeled DNA acting as signal amplifiers (**Figure 3C, Supplementary Figure 14**). We were especially interested in confirming the expected TOI surface distribution at the lowest probe density (0.5 probes/μm^2), where the sparsity of TOI molecules can ensure a maximum of one tether to the motor at any given time. Therefore, any detectable change in motor speed, either full stalling or transient stalling, at these low densities of probes would validate the single-molecule sensitivity of the turbo-charged motors. Furthermore, the frequency distributions of fluorescence intensities show an increase in average intensity and/or in pixel count with increasing

10.1002/anie.202316851

RESEARCH ARTICLE

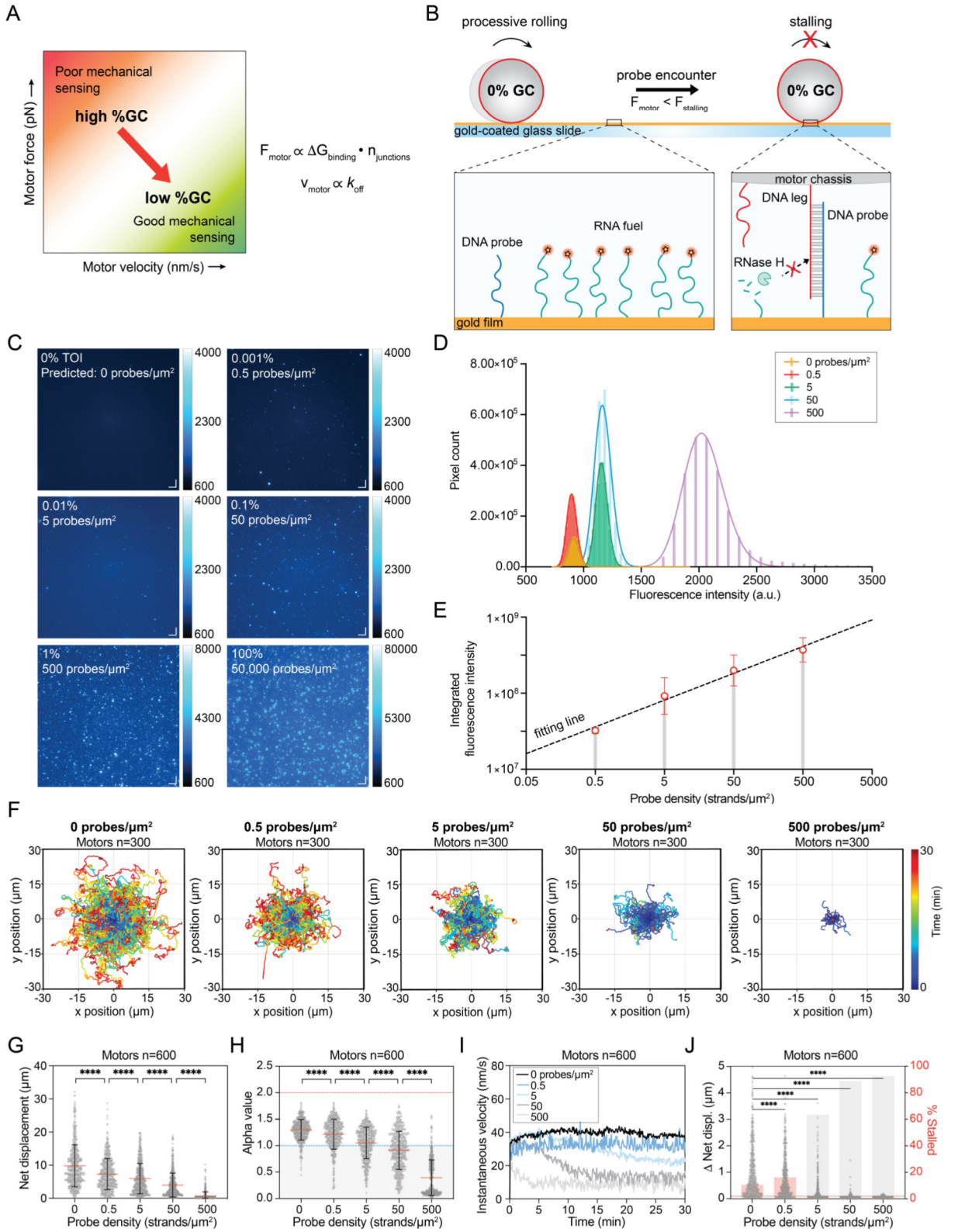

Figure 3. Using "turbo-charged" motors for single molecule sensing. A) Hypothetical plot of motor force vs. motor velocity shown with color depicting the predicted mechanical sensing capabilities. The motor force is proportional to $\Delta G_{binding}$ and the number of DNA:RNA junctions formed whereas the motor velocity is proportional to the rate of DNA:RNA unbinding, or k_{off}. B) Schematic of the DNA motor acting as a mechanical sensor and stalling upon DNA probe encounter. The motors roll on the RNA-coated chip and when they encounter a DNA probe that is complementary to the DNA-based motor leg, they bind to the probe and exhibit a stalling force as the RNase H enzyme does not cleave DNA:DNA duplexes. The motors will stall if the force of the motors is less than the force of the stalling. C) Representative fluorescence images showing DNA probes distribution at 0.5, 5, 50, 500 and 50,000 probes/μm² on the gold chip using ATTO647N-labeled spherical

nucleic acids as signal generators. Scale bar is 10 μm. D) Histogram plots of the fluorescence intensities (a.u.) for each DNA probe density. E) Plot of the integrated fluorescence intensity as a function of DNA probe density. The error bars represent the standard deviation from three separate regions across the microchannel. The best fit line is represented by Y=0.3518*X + 8.613 with an R^2 of 0.9861. F) Plots showing the trajectories of 300 motors on surfaces containing 0 probes/μm^2 which represents the control and 0.5, 5, 50, and 500 probes/μm^2. All the trajectories are aligned to the 0,0 (center) of the plots for time = 0 min. Color indicates time (0 →30 min). G) Plot showing net displacement of 600 motors on surfaces containing 0, 0.5, 5, 50, and 500 probes/μm^2. The error bars and the red lines represent the standard deviation and the mean of the distribution, respectively. H) Plot showing the α values of 600 motors on surfaces containing 0, 0.5, 5, 50, and 500 probes/μm^2. I) Plot showing the ensemble instantaneous velocity over time for 600 motors on surfaces containing 0, 0.5, 5, 50, and 500 probes/μm^2. **J)** Plots of the Δnet displacement as well as the percentage of motors stalled in the final 2 minutes of the 30-minute time lapse (*t*=28-30 min) for 600 motors on surfaces containing 0, 0.5, 5, 50, and 500 probes/μm^2. The red-dashed line represents the threshold (0.100 μm) used to calculate the percentage of stalled motors. **** indicates *P*<0.0001. Experiments were performed in triplicate.

TOI densities (**Figure 3D**). To account for the fluorescence 'bleed-through' of each particle across the neighboring pixels, we found that the integrated fluorescence intensity could provide clear evidence of an increasing trend in probe density (**Figure 3E**).

One caveat regarding the assay discussed above is that the target-induced dsDNA tethers might be susceptible to rupture if not engineered to withstand high mechanical stress. To address this issue, we maintained the same DNA legs on the motor surface, but we increased the number of base pairings between the DNA leg and the TOI (**Supplementary Figure 15**). We screened dsDNA tethers ranging from 15 to 18 bp in length. Our findings indicate that the motors exhibited the highest stalling efficiency when challenged by 17 bp dsDNA tethers, which displayed a significant increase in the percentage of stalled motors at the lowest TOI density (0.5 probes/μm^2) compared against the control surface without probes. Interestingly, our findings showed that the stalling efficiency dropped on surfaces presenting 18 bp dsDNA tethers. This could be ascribed to the longer time for molecular recognition and a slower hybridization rate for extended floppy DNA probes. Overall, this screening was pertinent to establishing the requirements for promoting the sensitivity of our DNA-based mechanosensor.

Given a bead-surface contact area of ~0.15 μm^2 and the measured speed of the motor, we calculated that τ (time to encounter) for 0.5 and 5 probes/μm^2 surfaces is achieved at ~11 min and ~1 min time intervals, respectively (**Supplementary Note 1**). When testing the motors on these different surfaces, we observed that the increasing ratio of surface-bound TOI progressively hampers the growth of motor trajectories (**Figure 3F**). Interestingly, the trajectories for 5 probes/μm^2 and greater showed abrupt stalling of the particles as indicated by red dots at the end of each trajectory which denotes the position and time of stalling (**Supplementary Figure 16**). The color in the trajectories indicates the time of the most recent particle position and hence stalling coincides with "red dots" (*t*=30 min) which is overlaid onto prior time points that have the same position. Further validating this data, we found that the net displacements were reduced as a function of probe density (**Figure 3G**). The α values of the ensembles also decreased as the TOI density increased, which is likely the result of how α is derived from the first 72 frames, and stalling leads to dampened α signaling physical constraints to the motion (**Figure 3H**). Note that motors without any addition of enzyme exhibit α of ~0.5. When we plotted the average instantaneous velocity for n=600 motors from triplicate measurement over time, we noted a decrease in the instantaneous velocity for increasing probe density (**Figure 3I**). The shape of these plots suggests that motors decelerate initially and then a subpopulation stall completely near the end of the time-lapse. The formation of non-hydrolysable dsDNA tethers is confirmed by the plateau in the average instantaneous velocity plots. This is particularly evident at higher densities of TOI (50 and 500 probes/μm^2), which can effectively decelerate or stall the motors within the first 5-10 minutes after enzyme addition. The change in net displacement as well as the significant increase in the percentage of stalled motors at the lowest probe density reflects the ability of turbo-charged motors to generate a discernible mechanical response to single TOI molecules, which is amplified as the density of TOI increases (**Figure 3J**).

The limit of detection (LOD) for our mechanosensing assay using turbo-charged motors was found to be 0.5 strands/μm^2 as surfaces presenting a lower density of TOI did not result in a statistically significant difference in net displacement and percentage of stalled motors (**Supplementary Figure 17**). At 0.05 probes/μm^2, the subpopulation of motors experiencing full or transient stalling is most likely too small to significantly lower the average net displacement for the entire population. Furthermore, our investigation into the effect of DNA leg density led to the finding that even a reduction of only ~14% in DNA leg density

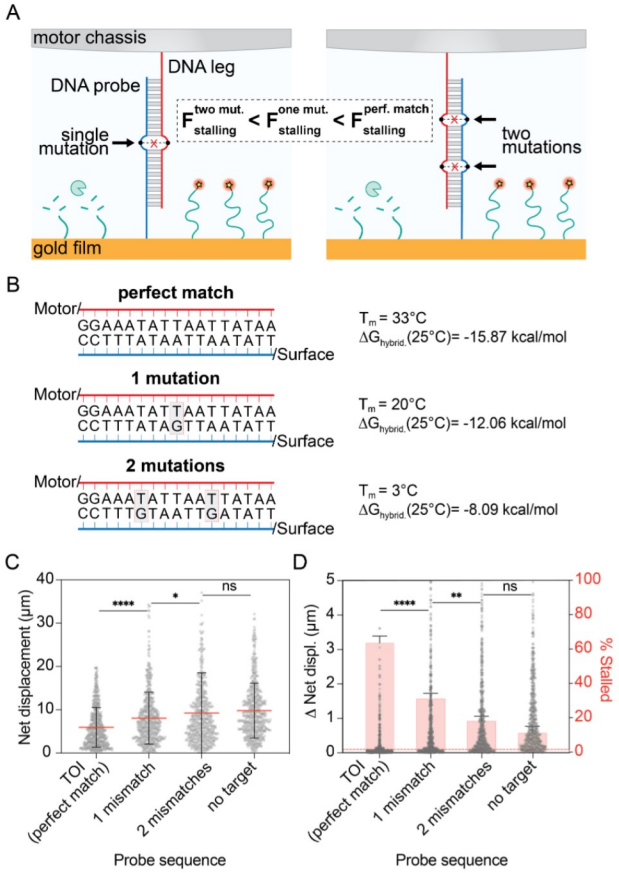

Figure 4. Specificity of the mechanical readout. A) Schematic illustrating the duplex formed between DNA legs and DNA probes presenting one and two mutations. B) Sequences of the DNA leg-DNA probe duplex presenting one and two mismatches with corresponding T_m and ΔG_{hybrid}, predicted using NUPACK. C) Plot showing net displacement of 600 motors on surfaces containing 5 probes/μm^2 with a perfect match, 1 and 2 mismatches to motor legs and no target. ****, * and ns indicate P<0.0001, P=0.0131 and not significant, respectively. The error bars and the red lines represent the standard deviation and the mean of the distribution, respectively. D) Plots of the Δnet displacement as well as the percentage of motors stalled in the final 2 minutes of the 30-minute time lapse (t=28-30 min). The red-dashed line represents the threshold (0.100 μm) used to calculate the percentage of stalled motors. ****, ** and ns indicate P<0.0001, P=0.0015 and not significant, respectively. Experiments were performed in triplicate.

causes a significant loss of sensitivity of the motors in detecting target nucleic acids (**Supplementary Figure 18**). The drastic increase in LOD with a decrease in DNA leg density underscores the importance of leg-target encounter events in mediating stalling. As the availability of DNA legs decreases, the encounter rate diminishes, consequently affecting the LOD.

Another important matter of concern for our mechanosensing assay is the specificity of the stalling event. We expect the high hybridization efficiency that comes with full complementarity between the motor legs and the TOI to be prerequisite for the generation of stalling forces by the bound DNA target molecules (**Figure 4A**). Predicted melting temperature and ΔG_{hybrid} values support the hypothesis that even one mismatch can significantly reduce the stability of the DNA leg-DNA probe duplex (**Figure 4B**). To test this, we introduced single-nucleotide and two-nucleotide mutations in the target and challenged the motors with a target density of 5 probes/μm^2. **Figure 4C** confirms that motor net displacements are significantly modified as a function of complementarity with the target. Consistently, a single mutation in the target DNA sequence cuts the percentage of stalled motors by approximately half, and probes with two mutations do not provide significant changes compared to the condition without the target (**Figure 4D**). Thus, our turbo-charged motors demonstrate single-nucleotide specificity, which is challenging for conventional assays and holds importance in genetic screening. Further evidence of the high specificity of turbo-charged motors comes from additional controls where we do not observe significant changes in motor displacement when encountering TOI with multiple mismatches at densities spanning from 0.5 to 500 probes/μm^2 (**Supplementary Figure 19**).

Conclusion

DNA-based constructs especially hold promise as the next-generation molecular machines because of their inherent ability to store and process chemical information.[30] In this paper, we explored the parameter space governing the dynamics of rolling DNA motors to generate a mechanosensor that productively transduces chemical information into a specific easy-to-detect mechanical output for the detection of single molecule concentrations of nucleic acids on a planar surface.

We demonstrated that the thermodynamic properties of the oligonucleotides involved in the translocation of rolling DNA motors substantially influence the kinetics of rolling, with ΔG_{hybrid} exerting the most control on k_{off} and thus the rate of forward stepping. When altering the duplexed leg length, we found that 15 bp duplexes between DNA legs and RNA fuel strands show the best compromise between speed and processivity, providing a starting point for further sequence space screening. Indeed, sequence optimization allowed us to design motors that serve as the best candidate for mechanical sensing of low concentrations of nucleic acids. Specifically, the 0% GC motors, or turbo-charged motors, match the translocation speeds of biological motor proteins without detaching from the track, which has been a major goal in the field. The weaker affinity of these DNA leg-RNA foothold interactions not only favors fast k_{off} but also low force generation, promoting the sensitivity of target-induced stalling mechanisms. We found evidence that turbo-charged motors can detect single DNA tethers as one binding event to the target oligonucleotide generates sufficient resistance to transiently or permanently stall the motor.

It is important that we also discuss a few drawbacks of our system. For example, RNA is sensitive to environmental RNases that will deplete the fuel and diminish motion which would not make it ideal for sensing. However, these issues can be addressed by the incorporation of RNase inhibitors. Another caveat is that in the current design of the motor sensor, we are limited in the choice of target, but this can be easily improved in future iterations as these motors are highly programmable. Nonetheless, this work highlights the high modularity and the single-molecule sensitivity of sensing assays mediated by rolling DNA motors. Also, fluorescence microscopy is exclusively used to perform control experiments, and we only need brightfield microscopy to read the mechanical output of our single-molecule assay. While we acknowledge the limitations of this construct in its current form, we envision future iterations being applied for sensing virtually any TOI in complex matrices and discriminating it among a variety of possible target molecules. Indeed, simple reprogramming of the motor sensors to integrate different types of molecular recognition elements such as antibodies, aptamers, or synthetic receptors could allow for the multiplexed detection of several other biomarkers, presenting intriguing applications in disease diagnostics.

Acknowledgements

We acknowledge support from NIH U01AA029345-01 (K.S.), NSF DMR 1905947 (K.S.), NSF MSN 2004126 (K.S.), Joachim Herz Stiftung Global Impact Award (S.P.), NIH NHLBI 3R01HL142866-04S1 (S.N.). We also thank Sergei Urazhdin for access to the thermal evaporator.

Conflicts of Interest

The authors declare no conflict of interest.

10.1002/anie.202316851

Data Availability Statement

The data that support the findings of this study will soon be available through DOI link.

Keywords: DNA nanotechnology · DNA motors · dynamic DNA machines · single molecule sensing

[1] M. Schliwa, G. Woehlke, *Nature* **2003**, *422*, 759-765.
[2] R. D. Vale, *Journal of Cell Biology* **1996**, *135*, 291-302.
[3] J. Bath, A. J. Turberfield, *Nature Nanotechnology* **2007**, *2*, 275-284.
[4] J.-S. Shin, N. A. Pierce, *Journal of the American Chemical Society* **2004**, *126*, 10834-10835.
[5] A.-K. Pumm, W. Engelen, E. Kopperger, J. Isensee, M. Vogt, V. Kozina, M. Kube, M. N. Honemann, E. Bertosin, M. Langecker, R. Golestanian, F. C. Simmel, H. Dietz, *Nature* **2022**, *607*, 492-498.
[6] J. Li, A. Johnson-Buck, Y. R. Yang, W. M. Shih, H. Yan, N. G. Walter, *Nature Nanotechnology* **2018**, *13*, 723-729.
[7] K. Yehl, A. Mugler, S. Vivek, Y. Liu, Y. Zhang, M. Fan, E. R. Weeks, K. Salaita, *Nature Nanotechnology* **2016**, *11*, 184-190.
[8] A. T. Blanchard, A. S. Bazrafshan, J. Yi, J. T. Eisman, K. M. Yehl, T. Bian, A. Mugler, K. Salaita, *Nano Letters* **2019**, *19*, 6977-6986.
[9] S. Piranej, A. Bazrafshan, K. Salaita, *Nature Nanotechnology* **2022**, *17*, 514-523.
[10] A. Bazrafshan, T. A. Meyer, H. Su, J. M. Brockman, A. T. Blanchard, S. Piranej, Y. Duan, Y. Ke, K. Salaita, *Angewandte Chemie International Edition* **2020**, *59*, 9514-9521.
[11] A. Bazrafshan, M.-E. Kyriazi, B. A. Holt, W. Deng, S. Piranej, H. Su, Y. Hu, A. H. El-Sagheer, T. Brown, G. A. Kwong, A. G. Kanaras, K. Salaita, *ACS Nano* **2021**, *15*, 8427-8438.
[12] S. Piranej, L. Zhang, A. Bazrafshan, M. Marin, G. B. Melikyan, K. Salaita, **2023**, bioRxiv preprint DOI: 10.1101/2023.02.27.530294.
[13] A. T. Blanchard, S. Piranej, V. Pan, K. Salaita, *The Journal of Physical Chemistry B* **2022**, *126*, 7495-7509.
[14] L. Samii, H. Linke, M. J. Zuckermann, N. R. Forde, *Physical Review E* **2010**, *81*, 021106.
[15] S. Kovacic, L. Samii, P. M. G. Curmi, H. Linke, M. J. Zuckermann, N. R. Forde, *IEEE Transactions on NanoBioscience* **2015**, *14*, 305-312.
[16] R. Pei, S. K. Taylor, D. Stefanovic, S. Rudchenko, T. E. Mitchell, M. N. Stojanovic, *Journal of the American Chemical Society* **2006**, *128*, 12693-12699.
[17] K. Lund, A. J. Manzo, N. Dabby, N. Michelotti, A. Johnson-Buck, J. Nangreave, S. Taylor, R. Pei, M. N. Stojanovic, N. G. Walter, E. Winfree, H. Yan, *Nature* **2010**, *465*, 206-210.
[18] P. Yin, H. Yan, X. G. Daniell, A. J. Turberfield, J. H. Reif, *Angewandte Chemie International Edition* **2004**, *43*, 4906-4911.
[19] S. J. Green, J. Bath, A. J. Turberfield, *Physical Review Letters* **2008**, *101*, 238101.
[20] J. Schnitzbauer, M. T. Strauss, T. Schlichthaerle, F. Schueder, R. Jungmann, *Nature Protocols* **2017**, *12*, 1198-1228.
[21] R. Jungmann, M. S. Avendaño, J. B. Woehrstein, M. Dai, W. M. Shih, P. Yin, *Nature Methods* **2014**, *11*, 313-318.
[22] M. G. L. van den Heuvel, C. Dekker, *Science* **2007**, *317*, 333-336.
[23] M. J. Schnitzer, K. Visscher, S. M. Block, *Nature Cell Biology* **2000**, *2*, 718-723.
[24] P. Pierobon, S. Achouri, S. Courty, A. R. Dunn, J. A. Spudich, M. Dahan, G. Cappello, *Biophysical Journal* **2009**, *96*, 4268-4275.
[25] B. Dybiec, E. Gudowska-Nowak, P. Hänggi, *Physical Review E* **2006**, *73*, 046104.
[26] H. Lee, H. Cho, J. Kim, S. Lee, J. Yoo, D. Park, G. Lee, *Nucleic Acids Research* **2022**, *50*, 1801-1814.
[27] H. H. Hogrefe, R. I. Hogrefe, R. Y. Walder, J. A. Walder, *Journal of Biological Chemistry* **1990**, *265*, 5561-5566.
[28] N. Srinivas, T. E. Ouldridge, P. Šulc, J. M. Schaeffer, B. Yurke, A. A. Louis, J. P. K. Doye, E. Winfree, *Nucleic Acids Research* **2013**, *41*, 10641-10658.
[29] A. J. Genot, D. Y. Zhang, J. Bath, A. J. Turberfield, *Journal of the American Chemical Society* **2011**, *133*, 2177-2182.
[30] Y. Benenson, T. Paz-Elizur, R. Adar, E. Keinan, Z. Livneh, E. Shapiro, *Nature* **2001**, *414*, 430-434.

10.1002/anie.202316851

WILEY VCH

RESEARCH ARTICLE

Entry for the Table of Contents

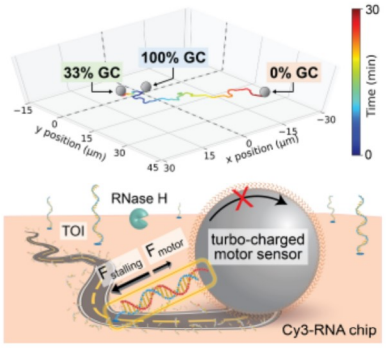

Programmable DNA motors with tunable properties. The 0% GC is the fastest motor and can detect and stall in the presence of single oligonucleotides.